ADVANCED OPTICAL MATERIALS
www.advopticalmat.de

Bioinspired Amyloid Nanodots with Visible Fluorescence

*Nadezda Lapshina, Ivan I. Shishkin, Ramesh Nandi, Roman E. Noskov, Hani Barhom, Sijo Joseph, Boris Apter, Tal Ellenbogen, Amir Natan, Pavel Ginzburg, Nadav Amdursky, and Gil Rosenman**

Nanoscale bioimaging is a highly important scientific and technological tool, where fluorescent (FL) proteins, organic molecular dyes, inorganic quantum dots, and lately carbon dots are widely used as light emitting biolabels. In this work, a new class of visible FL bioorganic nanodots, self-assembled from short peptides of different composition and origin, is introduced. It is shown that the electronic energy spectrum of native nonfluorescent peptide nanodots (PNDs) is deeply modified upon thermally mediated refolding of their biological secondary structure from native metastable to stable β-sheet rich structure. This refolding leads to the appearance of a broadband optical absorption across visible region and tunable, excitation-dependent visible FL of the nanodots with a high quantum yield of ≈30%. It is shown that this intriguing biophotonic effect appears in several peptides/proteins and does not require the presence of aromatic residues. It is assumed that the origin of the phenomenon is related to proton transfer along network of reconstructed intermolecular hydrogen bonds, stabilizing the thermally induced supramolecular β-sheet structure. The biocompatible FL PNDs can be potentially applied as high-resolution bioimaging labels toward advanced biotechnology and biomedical theranostics.

1. Introduction

Bioimaging is a principal method in biomedicine from local diagnosis and drug delivery to therapy and surgery.[1] It is mostly based on fluorescent (FL) agents of high brightness and combines exceptional optical properties with biocompatibility, biodegradability, and precise targeting both in vivo and in vitro. This includes inorganic semiconductor quantum dots,[2] carbon nanodots,[3] organic molecular dyes,[4] and genetically encoded universal FL proteins.[5] Additional specific class of extrinsic FL nanoprobes is amyloid-binding small molecule ligands (thioflavin T, Congo red and more) employed for tracking the kinetics of amyloid fibrils growth.[6] Each of the imaging agents has its inherent mechanism of photon emission, which defines its figures of merit for bioimaging: FL spectral region, quantum yield (QY), and photobleaching.[7,8] For instance, quantum dots and organic dye molecules exhibit FL in the visible range and have very high QY exceeding 90%. However, the organic molecular dyes are limited for long-term bioimaging applications because of photobleaching issues. The biocompatibility is another basic parameter of any biolabels, which is especially critical for some organic dyes and inorganic semiconductor quantum dots, containing heavy metals. Recently found FL carbon nanodots are biocompatible but have a low QY.[9] The green fluorescence protein (GFP) and its homologues are the only molecules, known until today, having biological origin FL and providing unique biocompatibility. These proteins exhibit pronounced FL with QY reaching 90% covering the entire visible spectrum, which makes them unique FL tags[10] among unlimited number of nonfluorescent peptide and protein biomolecules.[1,2,5,7]

Alternative composition-insensitive visible FL was recently found in biological and bioinspired nanostructures characterized by specific ordering of biomolecules into antiparallel β-sheets structures. This includes a wide variety of diverse biomolecular compositions, such as amyloidogenic proteins,[11,12] PEGylated peptides,[13,14] nonaromatic biogenic, and synthetic peptides[15] and recently natural silk fibrils.[16] The basic features of these FL nanostructures are similar fibrillar morphology, original β-sheets secondary structure, and identical visible FL optical spectrum. These common structural and optical properties enable to relate all of them to a wide class of thermodynamically stable disease- and nondiseased-related amyloid structures.[17–19] Such β-sheet structures and visible FL can also

N. Lapshina, Dr. I. I. Shishkin, Dr. R. E. Noskov, H. Barhom, Dr. S. Joseph, Prof. T. Ellenbogen, Dr. A. Natan, Dr. P. Ginzburg, Prof. G. Rosenman
School of Electrical Engineering
Faculty of Engineering
Tel Aviv University
Ramat Aviv
Tel Aviv 6139001, Israel
E-mail: gilr@eng.tau.ac.il
R. Nandi, Prof. N. Amdursky
Schulich Faculty of Chemistry
Technion – Israel institute of Technology
Technion City, Haifa 3200008, Israel
Dr. B. Apter
Faculty of Engineering
Holon Institute of Technology
52 Golomb st., POB 305, Holon 5810201, Israel
The ORCID identification number(s) for the author(s) of this article can be found under https://doi.org/10.1002/adom.201801400.

DOI: 10.1002/adom.201801400

be created in ultrashort di- and tri-peptide nanostructures[20] which are originally nonfluorescent in the visible range.[21] It was shown[20] that both aromatic and nonaromatic peptide nanostructures are subjected to thermally mediated refolding of their secondary structure accompanied by full reconstruction of their native morphology (nanotubes, nanospheres) to β-sheets ultrathin fibrils. This reconstructive transition of the first order[20] was accompanied by visible FL properties,[20,22] similar to those observed in amyloid and nonamyloid originally β-sheets structures[11–16] demonstrating the same optical spectrum of FL regardless of their nature and composition.

In this work, we apply the latter new paradigm for generating new class of bioinspired peptide/protein nanodots possessing intense and tunable fluorescence in the visible region. We use originally nonfluorescent peptides/proteins that are transformed into visible FL nanoparticles using thermally induced refolding of their initial biomolecular secondary structure from native metastable state to β–sheet phase. The main advantages of the developed FL peptide nanodots (PNDs) with respect to existing bioimaging agents include highly monodisperse size distribution with the average value ranging from 1 to 10 nm, biocompatibility, and visible widely tunable fluorescence within the wavelength domain 420–650 nm.

2. Results and Discussion

The fabrication process of visible nanodots consists of two steps. At the first step, PNDs were self-assembled from monomer peptide molecules in organic solvents by a bottom-up method developed in our works,[23,24] where the peptide/protein monomer nucleates to seeds with a critical size, which can be considered as building blocks in terms of the supramolecular concept. Later, these PNDs can undergo further self-assembly to nano- or microstructures of diverse morphologies driven by weak noncovalent interactions. In our study, we inhibited these self-assembly process of native di- and tri-peptide biomolecules at the first initial stage of nucleation to nanodots by the use of polar solvents. At the second step, the PNDs were subjected to a thermal treatment at 160 °C in high boiling temperature solvent of ethylene glycol (EG) to transform the nonfluorescent PNDs to visible FL PNDs with a refolded secondary structure. We studied four different monomer biomolecules of dissimilar origin as representatives of different peptide groups: aromatic di- and tri-phenylalanine (FF and FFF), aliphatic di-leucine (LL), and the insulin protein.

High-resolution microscopy techniques, namely atomic force microscopy (AFM), environmental scanning electron microscopy (ESEM), and transmission electron microscopy (TEM) were exploited for morphological analyses of the PNDs. The images of the FFF-PNDs are demonstrated in **Figure 1** (morphological data for the other PNDs can be found in Figures S1 and S2 in the Supporting Information), which shows individual FFF-PND with an average height and lateral dimensions of ≈10 nm (Figure 1a–c). Inspection of our other PND (FF and LL PND) showed lower dimensions ≈3 nm (Figure S2, Supporting Information).

The optical properties of optical absorption (OA), FL spectroscopy, and FL lifetime were studied for native and thermally treated FFF-PNDs, where a profound difference between before and after the thermal treatment was observed (**Figure 2**). The OA for native FFF-PNDs (Figure 2a) has its absorption edge in the region of $\lambda \approx 250$–270 nm which is similar to those observed in peptide nanostructures, such as FF-nanotubes, FFF-nanospheres, and FFF-nanoplates.[20–22] This OA is associated with the aromatic benzoic ring of the phenylalanine residues.[25] It should be noted that aliphatic leucine amino acid and native LL-peptide nanodots, nanotubes, and nanofibers do not demonstrate any OA in this UV spectral interval.[20,25] Thus, both F-aromatic and L-aliphatic based PNDs in their native states are entirely transparent in a wide optical region covering visible and near IR regions (Figure 2a).

Native FFF-PND exhibit FL in the UV region (Figure S3, Supporting Information) at $\lambda \approx 290$ nm, as similar for all phenylalanine-based nanostructures,[20] which originate from its benzoic rings.[25] In contrast, the aliphatic leucine–based LL-nanostructures do not generate any FL effect in the UV range. Thermal treatment of the studied self-assembled PNDs led to a transition in their optical properties. The OA spectrum (Figure 2a) of the heated FFF-nanodots (red graph) demonstrates a new broad OA band covering the entire visible region, which leads to new FL properties (Figure 2b). The most distinguished feature of this acquired FL effect is its excitation dependence, making FL tunable in a very wide visible range from deep blue (420 nm) to red (650 nm) (Figure 2b,c). It is also illustrated by linear graph of FL peaks versus excitation wavelengths (Figure 2c) and inset at Figure 2c of several color FL images of heated FFF-nanodots excited by different wavelengths. In addition, to understand

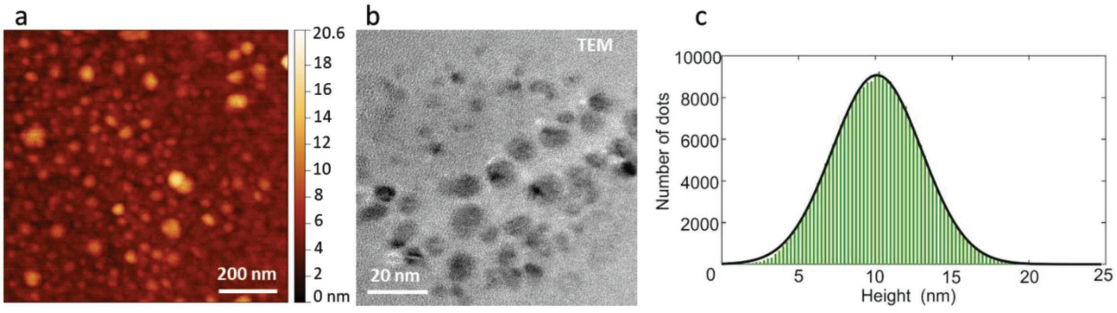

Figure 1. Morphological characterization of FFF-nanodots. a,b) AFM and TEM images of self-assembled FFF-nanodots, respectively. c) Height distribution of FFF-nanodots obtained from AFM measurement representing the average *Z*-dimension of ≈10 nm. According to TEM characterization, the average *X*–*Y* dimension is ≈10 nm.

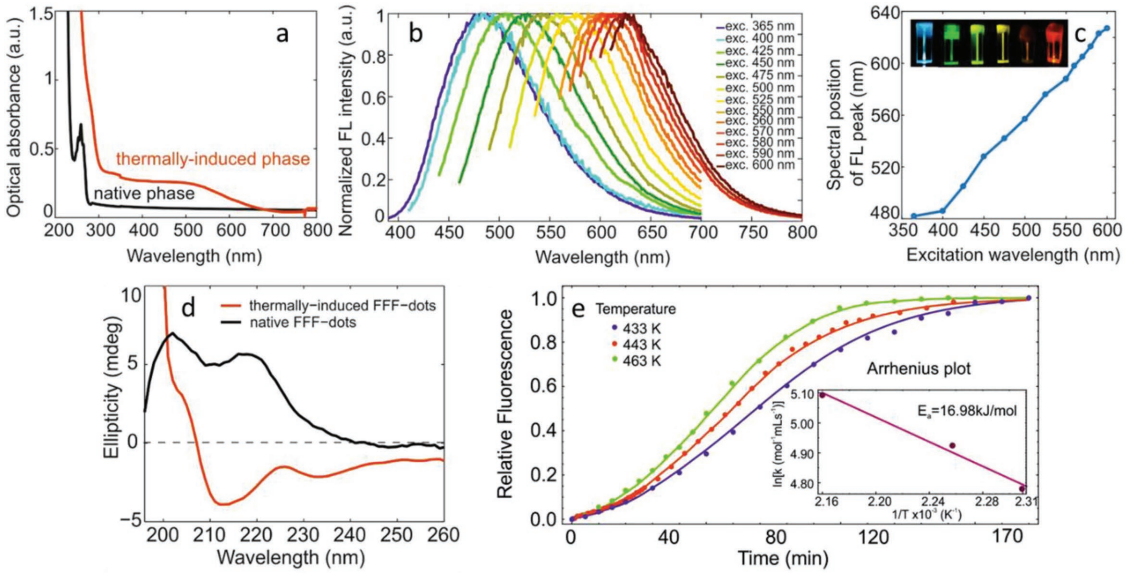

Figure 2. Optical properties of native and thermally treated FFF-nanodots. a) OA of native (black line) and thermally treated (red line) nanodots. b) Normalized FL spectra of thermally treated nanodots versus the excitation wavelength, λ_{exc}, varied in the range 365–600 nm. c) The FL photon emission peak versus λ_{exc}. Inset shows color images of thermally treated FFF-nanodots at different excitation wavelengths (from left to right: λ_{exc} = 360 nm, λ_{exc} = 450 nm, λ_{exc} = 510 nm, λ_{exc} = 530 nm, λ_{exc} = 570 nm, λ_{exc} = 590 nm) demonstrating continuous variation of the FL spectrum. d) CD spectra of FFF-nanodots in native (black line) and thermally induced (red line) phases illustrating a transition from helical to β-sheet secondary structure. e) Monitoring of the refolding kinetics in FFF-nanodots by FL measurements at three different temperatures of the heat treatment (433, 443, and 463 K). The excitation and emission FL wavelengths were 404 and 530 nm, respectively. Fitting of the experimental data was performed in accordance with Arrhenius equation (Equation (1)). The inset shows the reaction rate (in the log scale) versus the inverse temperature. It allows the linear fitting that gives an activation energy of 16.98 kJ mol^{-1} and frequency factor A = 13 500 mol^{-1} mLs^{-1}.

whether the process of intrinsic FL is linear or not, we measured the Stokes signal (peak FL line) as a function of the excitation laser input power. This dependence (Figure S6, Supporting Information) clearly shows that the observed FL in our nanodots is a linear process. Measured QY of FFF-dots in the blue region ($\lambda_{exc} \approx$ 380 nm, $\lambda_{em} \approx$ 460 nm) showed relatively high value QY of ≈30%. Regardless of original composition, similar FL properties were also observed both for aromatic FF- and aliphatic LL-PNDs subjected to heat treatment (Figure S4, Supporting Information). It should be reminded that dimensions of FF- and LL-nanodots (Figure S2, Supporting Information) are smaller by a factor of ≈3–4 than those of FFF-dots (Figure 1) though they demonstrate similar FL spectra. Found similarity of FL properties from PNDs of different composition, origin, and dimensions implies that structural biomolecular reorganization of the PNDs upon heat treatment is probably the reason for the FL properties.

The latter assumption is supported by our circular dichroism (CD) measurement of the peptide secondary structure.[26] Before heat treatment, the CD spectrum of the native FFF-PNDs (Figure 2c, blue line) exhibits two positive molar ellipticity maxima at 203 and 219 nm. Such CD spectrum is consistent with a left-handed α-helix, where our observed peaks correspond to π–π^* and n–π^* electronic transitions, respectively.[27,28] Though it is commonly thought that small linear peptides of 3–6 amino acids cannot exhibit α-helical conformation due to size restrictions, an ability of such ultrasmall peptides to form α-helical structures upon crossing a threshold concentration was recently shown.[29,30] Following thermal treatment of the FFF-PNDs, the CD spectrum changes dramatically, and it becomes negative with ellipticity minimum at 214 nm (Figure 2c, red line). This negative peak is consistent with an antiparallel β-sheet secondary structure.[11,31–33] In addition to CD, another method of Fourier transform infrared (FTIR) spectroscopy is widely used in biology to study biomolecular conformation. It was recently shown by both CD and FTIR[22] that the same thermally induced refolding from initial α-helical conformation to β-sheet arrangement happens in FFF-tapes. It is important to stress that, according to the biological supramolecular concept, any peptide structures are composed from the same building blocks which we define as nanodots. That is why FTIR results obtained for FFF-tapes can be applied to FFF-nanodots as well. Hence, our CD measurements clearly show a structural transition of the FFF-PNDs from helical conformation to a new β-sheet secondary structure. Similar conformational transition from α-helix to β-sheet secondary structure is well-known and observed in protein/peptide misfolding and subsequent β-sheet rich amyloid fibril-like structure formation.[34–37] Protein fibrils consisted of β-sheets under fibrillization process become thermodynamically stable with respect to their native state.[34,38]

As in any other (biological) structural transition, such thermo-activated processes are associated with their own set of kinetic rates. FFF-nanodots in their initial helical phase were heated fast to chosen elevated temperatures. The conformational rate from initial metastable α-helix to FL β-sheets was monitored by the relative FL intensity (excitation λ_{exc} = 404 nm, emission λ_{exc} = 530 nm) as a function of time at three different temperatures 433, 443, 463 K (Figure 2e). Such a classical approach allows to extract the natural activation energy barrier, associated with the transition to the β-sheet structure upon

heat treatment. The analysis of our observed thermally induced transition can be performed in the framework of the standard autocatalytic model[39], which can be written as:

$$\frac{dP_\alpha}{dt} = -kP_\beta P_\alpha$$
$$\frac{dP_\beta}{dt} = kP_\beta P_\alpha, \quad (1a)$$

where P_α and P_β denote the relative aggregate concentration in α-helix and β-sheet phases, respectively, and k stands for the reaction rate. The solution of these equations is given by:

$$P_\alpha(t) = \frac{1}{1 + \frac{P_{\beta 0}}{P_{\alpha 0}} \exp(-kt)}$$
$$P_\beta(t) = 1 - P_\alpha(t) \quad (1b)$$

with $P_{\alpha 0}$ and $P_{\beta 0}$ corresponding to the initial relative aggregate concentration, where $P_{\alpha 0} + P_{\beta 0} = 1$. Within this model, we assume that the concentration of the FFF-nanodots is invariant while the transitions concern their internal structure only.

Fitting experimental data with Equation (1), shown in Figure 2, allowed us to retrieve the initial aggregate concentrations of $P_{\alpha 0} = 0.91$ and $P_{\beta 0} = 0.09$ for all samples under the study. Plotting the extracted logarithm of the reaction rates at different temperatures as function of inverse temperature (inset of Figure 2e) allowed the fitting to the Arrhenius equation:

$$k = A \exp\left(-\frac{E_a}{RT}\right) \quad (2)$$

where the frequency factor A accounts for the frequency of collisions, E_a is the activation energy, and R the gas constant. The value of A has been obtained from the Arrhenious plot, accounting for the fact that the initial concentration of monomers is 1 mg mL^{-1} and their molar mass is 459.55 g mol^{-1}.[40] Our fitting results in the activation energy of $E_a = 16.98$ kJ mol^{-1} and the frequency factor for the transitions of $A = 13\ 500$ mol^{-1} mLs^{-1}. Interestingly, our calculated activation energy is around 2–3 fold lower than the calculated activation energy for amyloid fibril elongation process, which also involves a transition to β-sheet structures.[39]

The similarity in the kinetics profile between our findings to the natural process undergone by amyloid fibrils has encouraged us to explore whether we can see similar optical phenomenon as we see for the FFF-, FF-, and LL-nanodots, but with amyloid-forming protein. We have chosen insulin as a common protein model for amyloidogenic protein, i.e., protein that can form amyloid structures. We used the same protocol as for the formation of the FFF-, FF-, and LL-nanodots, meaning that we inhibited the amyloidogenesis process after the formation of the first nuclei. As can be seen in **Figure 3**, the OA (Figure 3a) and FL (Figure 3b) of insulin have similar characteristics to the ones of the FFF nanodots, i.e., the appearance of visible absorbance and excitation-dependent emission spectrum upon thermal heating. Furthermore, we also observe rather similar structural transition of insulin from a predominant α-helical structure to a β-sheet–rich structure after heating (Figure 3c). Our measurements with the insulin protein highly support our assumption regarding the unique origin of electronic structure and FL in the nanodots.

Strong composition-insensitive FL effect found in the visible region for the heat treated β-sheet peptide/protein nanodots of different origin (Figures 2b,c, 3b) is the direct evidence of a deep reconstruction of the dots' electronic energy levels structure. Using FL excitation (FLE) spectra at different FL wavelengths, λ_{em}, allowed us to represent our data in the form of Jablonski diagram (**Figure 4**), which demonstrates the energy states of the FFF-PNDs and the transitions between them. In order to demonstrate behavior of several FLE configurations (for blue, green, and red), a set of thee Jablonski diagrams, including three levels each, were reconstructed. The experimental absorption spectra (level broadening) of the upper states appear in in the figure next to the upper level sign. Phenomenologically speaking, an excited electron undergoes nonradiative transition to the lower level, which is connected via dipolar transition (experimentally acquired ns-scale lifetimes support this hypothesis) back to the ground state. Both excitation and emission spectra have close to Gaussian shapes, suggesting considerable inhomogeneous broadening in the macroscopic assembly of emitters.

Fluorescence lifetime studies (**Figure 5**a–c) of the FFF-nanodots taken at different excitation wavelengths ($\lambda_{exc} = 404$, 450, and 550 nm) reveal that the FL decay is multiexponential which was fitted with a superposition of three exponential functions. The dominant contribution is given by the function with the shortest lifetime which decreases as the excitation wavelength growths (Figure 5), leading to narrowing of the emission line (Figure 4).

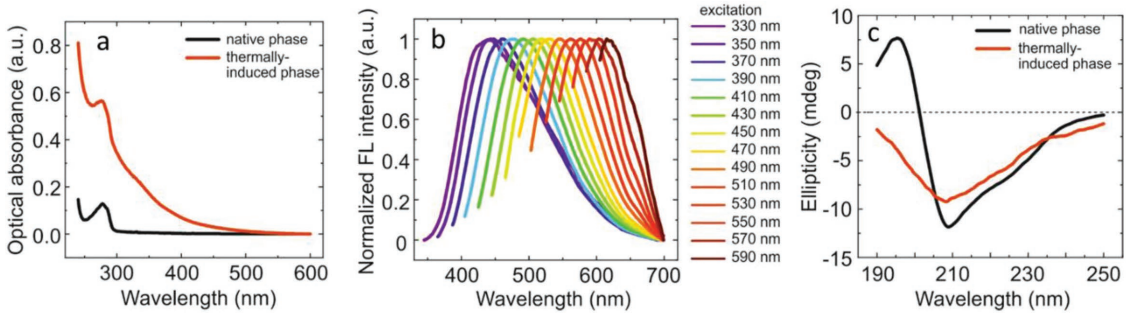

Figure 3. Optical properties of insulin. a) OA of insulin before (black curve) and following thermal treatment (red curve). b) Fluorescence spectrum of thermally induced insulin as a function of the excitation wavelength. c) CD of insulin before (black curve) and following thermal treatment (red curve).

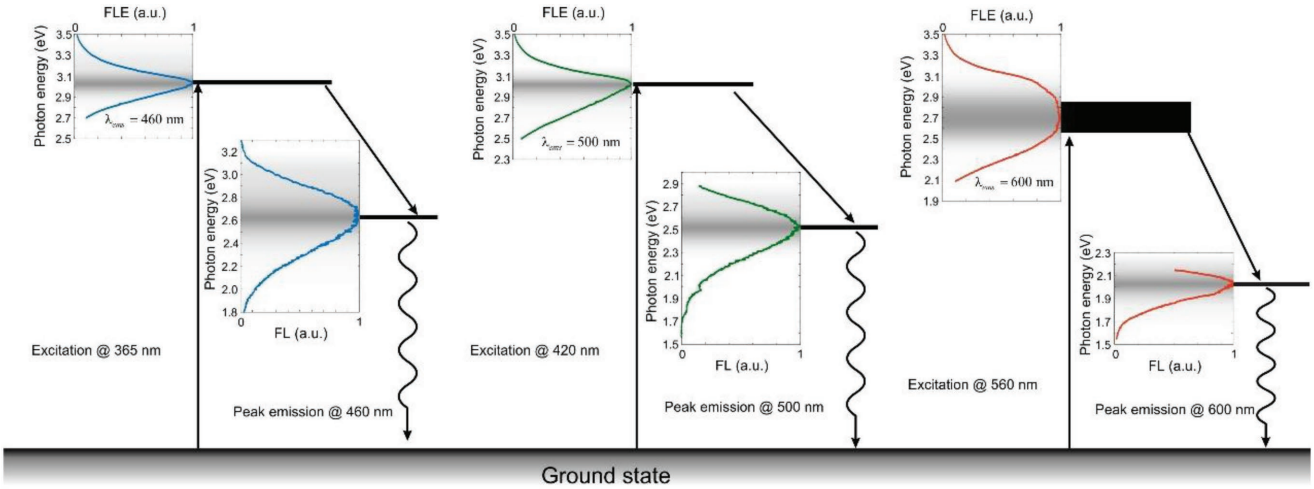

Figure 4. Jablonski diagram illustrating the energy states of the peptide dots and the transitions between them. Straight and squiggly arrows indicate nonradiative and radiative transitions, respectively. Top insets denote PL excitation spectra at the emission wavelengths of 460, 500, and 600 nm. Bottom inserts show FL spectra at the excitation wavelength of 365, 420, and 560 nm. Shading indicates the density of states.

Several explanations were considered for the mechanism of visible FL in nanostructures that are composed of self-assembled short peptides and proteins. A leading hypothesis is that the hydrogen bonds in β-sheet rich structures, that play a critical role in stabilizing the secondary structure, are also very important in the FL processes.[11–13,19,32,33] Those bonds were considered to induce either additional electron delocalization or change the electronic structure significantly to allow such an excited state effect. This hypothesis involves a proton transfer between *C* and *N* terminals of the intermolecular hydrogen bonds, i.e., between two molecules that are connected through a hydrogen bond (β-strands in the structure of cross β-sheets). This proton transfer can happen in the S_1 first excited state, but also in S_2, S_3, or even higher excited states, hence leading to the possibility of getting FL over a range of possible colors that will generally depend on the detailed spectrum of the molecules in both ground state and excited state geometry. The latter concept is illustrated in Figure 5d with a possible Frank–Condon diagram that involves proton transfer in higher excited states and can lead to multicolor excitation-dependent FL. The possibility of excited state proton transfer involvement in FL can be observed in a wide range of systems,[20,41] including GFP. Quantum molecular modeling (DFT and TDDFT simulations) showed that proton transfer can induce gap reduction in several self-assembled peptide structures.[42]

In addition, it is also important to distinguish between our observed visible FL effect to the one of exciton confinement induced by an alternation of nanoparticles dimensions, i.e., as in quantum dots. Excitons in quantum dots are defined by Coulomb interactions between electrons and holes. In organic and bioorganic materials, where electrostatic interaction is very strong, Frenkel exciton is the predominant one. In this case, electron–hole pair is localized at the same molecule at the distance of 10–20 Å from each other and its binding energy is very large, ≈1 eV. Due to its spatial limitation, it is not feasible to confine spatially such small excitons. This conclusion is supported by our experimental results where much larger FFF-dots having ≈10 nm dimensions than 2–3 nm size of FF- and LL-ones exhibit similar FL spectra.

Our thermally treated visible PNDs have several attractive properties, such as multicolor emission profile, small nanometer size, and potential biocompatibility[43] which make them compelling candidates for fluorescence bioimaging. Moreover, our peptide/protein nanodots exhibit excellent photostability, as can be seen in our photobleaching measurements (**Figure 6**a). As a proof-of-principle for the use of the FFF-nanodots for bioimaging, we embedded them into

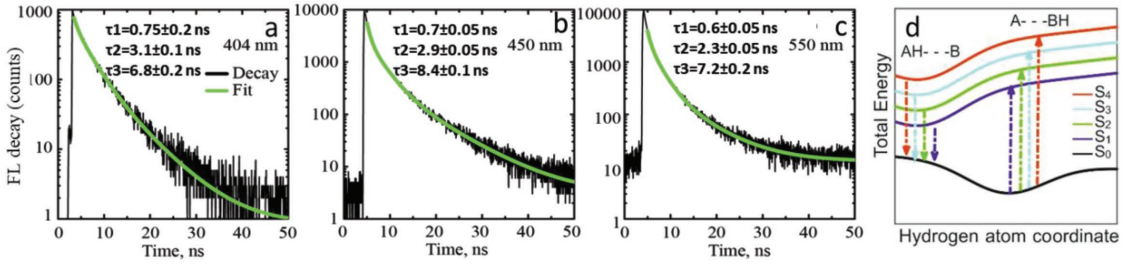

Figure 5. a–c) FL lifetimes at λ_{exc} = 404 nm, λ_{exc} = 450 nm, and λ_{exc} = 550 nm, respectively. d) Frank–Condon diagram showing the possible effect of proton transfer on electronic properties. After excitation, a spatial relocation of proton along hydrogen bond leads to a lower bandgap and hence fluorescence at longer wavelengths.

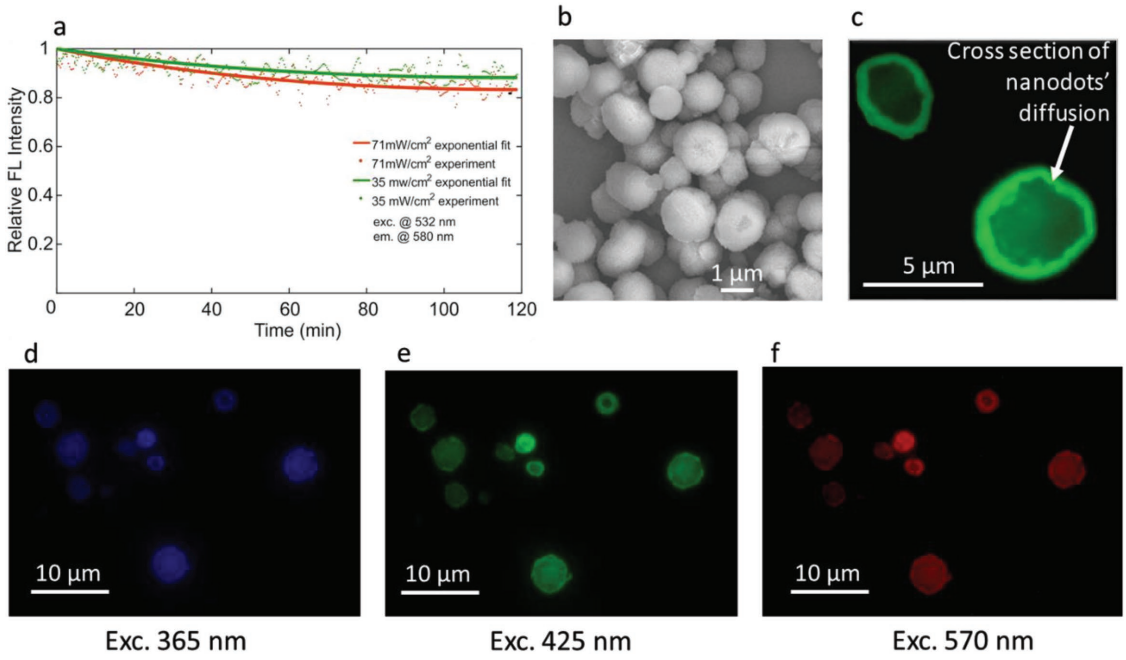

Figure 6. Demonstration of photostability and compatibility with vaterite microcapsules for targeted delivery for FFF-bionanodots. a) Relative FL intensity at 580 nm versus time illustrating good photostability. λ_{exc} of 532 nm, taken with a continuous wave (CW) laser at power densities of 71 mW cm^{-2} (red curve) and 35 mW cm^{-2} (green curve). b) ESEM image of porous vaterite microspheres. c) Fluorescence microscopy image of two vaterite particles with FFF-nanodots embedded their pores representing cross section of nanodots diffused nonuniformly. d–f) Imaging of vaterite spheres in blue, green, and red spectral regions due to intrinsic fluorescence of embedded nanodots (λ_{exc} = 365 nm, λ_{exc} = 425 nm, and λ_{exc} = 570 nm).

porous vaterite semispherical particles of micron-scale size, which are widely used in medical applications as a cargo for drug delivery[44,45] (Figure 6b,c). FL microscopy images of the FFF-labeled vaterite microparticles under different excitation wavelength (Figure 6d–f) demonstrate their ability to serve as multicolor FL agents.

3. Conclusion

In conclusion, we present here a new type of bionanodots self-assembled from peptides/proteins of different origin and complexity such as ultrashort peptides and amyloid insulin protein. Despite the deep difference, all of them demonstrate similar and tunable excitation-dependent fluorescence for the entire visible range. We show that this transition from a nonfluorescent to bright visible nano-objects is accompanied with a structural transition from an α-helical structure to a β-sheet-rich one. We further use an amyloidogenic protein to show that this structural transition can be compared to structural transformation occurring during the amyloidogenesis process, and vice versa, that amyloidogenic protein can exhibit similar optical properties as our thermally induced FL bionanodots assembled from simple ultrashort di- and tri-peptides. The main advantages of our proposed visible nanodots with respect to existing bioimaging agents include their highly homogenous ultrasmall size of several nanometers, original biocompatibility, and intensive tunable visible fluorescence. This new generation of visible nanodots can be used in nanobiotechnology, for medical diagnostics, and therapy and can dramatically impact additional nanotechnological fields such as image sensors, light emitting devices, display technology and more.

Supporting Information

Supporting Information is available from the Wiley Online Library or from the author.

Acknowledgements

This project was supported by Ministry of Science, Technology and Space of Israel. The authors thank Dr. Zahava Barkay for help with ESEM measurements, Dr. Artium Khatchatouriants for AFM studies, and Dr. Daniel Szwarcman for quantum yield measurements.

Conflict of Interest

The authors declare no conflict of interest.

Keywords

fluorescent peptide nanodots, peptide nanophotonics, peptide nanostructures, refolding of peptide secondary structure, visible fluorescence

Received: October 14, 2018
Revised: December 2, 2018
Published online: December 28, 2018

[1] O. S. Wolfbeis, *Chem. Soc. Rev.* **2015**, *44*, 4743.
[2] A. P. Alivisatos, *Science* **1996**, *271*, 933.
[3] A. Sharma, T. Gadly, S. Neogy, S. K. Ghosh, M. Kumbhakar, *J. Phys. Chem. Lett.* **2017**, *8*, 1044.
[4] M. J. Schnermann, *Nature* **2017**, *9*, 176.
[5] D. M. Chudakov, M. V. Matz, S. Lukyanov, K. A. Lukyanov, *Physiol. Rev.* **2010**, *90*, 1103.
[6] C. W. Bertoncini, M. S. Celej, *Curr. Protein Pept. Sci.* **2011**, *12*, 206.
[7] B. R. Smith, S. S. Gambhir, *Chem. Rev.* **2017**, *117*, 901.
[8] M. V. Kovalenko, L. Manna, A. Cabot, Z. Hens, D. V. Talapin, C. R. Kagan, V. I. Klimov, A. L. Rogach, P. Reiss, D. J. Milliron, P. Guyot-Sionnnest, G. Konstantatos, W. J. Parak, T. Hyeon, B. A. Korgel, C. B. Murray, W. Heiss, *ACS Nano* **2015**, *9*, 1012.
[9] Y. Wang, Y. Zhu, S. Yu, C. Jiang, *RSC Adv.* **2017**, *7*, 40973.
[10] N. C. Shaner, G. H. Patterson, M. W. Davidson, *J. Cell Sci.* **2007**, *120*, 4247.
[11] F. T. Chan, G. S. Kaminski Schierle, J. R. Kumita, C. W. Bertoncini, C. M. Dobson, C. F. Kaminski, *Analyst* **2013**, *138*, 2156.
[12] D. Pinotsi, A. K. Buell, C. M. Dobson, G. S. Kaminski Schierle, C. F. Kaminski, *ChemBioChem* **2013**, *14*, 846.
[13] C. Diaferia, T. Sibillano, N. Balasco, C. Giannini, V. Roviello, L. Vitagliano, G. Morelli, A. Accardo, *Chem. - Eur. J.* **2016**, *22*, 16586.
[14] C. Diaferia, T. Sibillano, N. Balasco, C. Giannini, V. Roviello, L. Vitagliano, G. Morelli, A. Accardo, *Chem. - Eur J.* **2017**, *23*, 14309.
[15] R. Ye, Y. Liu, H. Zhang, H. Su, Y. Zhang, L. Xu, R. Hu, R. T. K. Kwok, K. S. Wong, J. W. Y. Lam, W. A. Goddard, B. Z. Tang, *Polym. Chem.* **2017**, *8*, 1722.
[16] U. Shimanovich, D. Pinotsi, K. Shimanovich, N. Yu, S. Bolisetty, J. Adamcik, R. Mezzenga, J. Charmet, F. Vollrath, E. Gazit, C. M. Dobson, G. Kaminski Schierle, C. Holland, C. F. Kaminski, T. P. J. Knowles, *Macromol. Biosci.* **2018**, *18*, 1700295.
[17] J. I. Guijarro, M. Sunde, J. A. Jones, I. D. Campbell, C. M. Dobson, *Proc. Natl. Acad. Sci. USA* **1998**, *95*, 4224.
[18] G. Wei, Z. Su, N. P. Reynolds, P. Arosio, I. W. Hamley, E. Gazit, R. Mezzenga, *Chem. Soc. Rev.* **2017**, *46*, 4661.
[19] T. P. J. Knowles, M. Vendruscolo, C. M. Dobson, *Phys. Today* **2015**, *68*, 36.
[20] A. Handelman, N. Kuritz, A. Natan, G. Rosenman, *Langmuir* **2016**, *32*, 2847.
[21] N. Amdursky, P. Beker, I. Koren, B. Bank-Srour, E. Mishina, S. Semin, T. Rasing, Y. Rosenberg, Z. Barkay, E. Gazit, G. Rosenman, *Biomacromolecules* **2011**, *12*, 1349.
[22] A. Handelman, N. Lapshina, B. Apter, G. Rosenman, *Adv. Mater.* **2018**, *30*, 1705776.
[23] N. Amdursky, E. Gazit, M. Molotskii, G. Rosenman, *J. Am. Chem. Soc.* **2010**, *132*, 15632.
[24] N. Amdursky, E. Gazit, G. Rosenman, *Biochem. Biophys. Res. Commun.* **2012**, *419*, 232.
[25] J. R. Lakowicz, *Principles of Fluorescence Spectroscopy*, Plenum Press, NY, USA **1983**.
[26] I. W. Hamley, *Angew. Chem., Int. Ed.* **2007**, *46*, 8128.
[27] H. N. Hoang, G. Abbenante, T. A. Hill, G. Ruiz-Gomez, D. P. Fairlie, *Tetrahedron* **2012**, *68*, 4513.
[28] K. O. Nakanishi, N. Berova, R. Woody, *Circular Dichroism: Principles and Applications*, VCH, New York **1994**.
[29] N. Amdursky, M. L. Stevens, *ChemPhysChem* **2015**, *16*, 2768.
[30] C. A. E. Hauser, R. Deng, A. Mishra, Y. Loo, U. Khoe, F. Zhuang, D. W. Cheong, A. Accardoc, M. B. Sullivan, C. Riekel, J. Y. Ying, U. A. Hauser, *Proc. Natl. Acad. Sci. USA* **2011**, *108*, 1361.
[31] K. E. Marshal, L. C. Serpel, *Biochem. Soc. Trans.* **2009**, *37*, 671.
[32] A. Shukla, S. Mukherjee, S. Sharma, V. Agrawal, K. V. Radha Kishan, P. A. Guptasarma, *Arch. Biochem. Biophys.* **2004**, *428*, 144.
[33] D. Pinotsi, A. K. Buell, C. M. Dobson, G. S. Kaminski Schierle, C. F. Kaminski, *ChemBioChem* **2013**, *14*, 846.
[34] C. M. Dobson, *Philos. Trans. R. Soc. B* **2001**, *356*, 133.
[35] A. L. Fink, *Folding Des.* **1998**, *3*, R9.
[36] H. Mihara, Y. Takahashi, *Curr. Opin. Struct. Biol.* **1997**, *7*, 501.
[37] H. Mihara, Y. Takahashi, *Biopolymers* **1998**, *47*, 83.
[38] A. J. Baldwin, T. P. J. Knowles, G. Gaetano Tartaglia, A. W. Fitzpatrick, G. L. Devlin, S. L. Shammas, C. A. Waudby, M. F. Mossuto, S. Meehan, S. L. Gras, J. Christodoulou, S. J. Anthony-Cahill, P. D. Barker, M. Vendruscolo, C. M. Dobson, *J. Am. Chem. Soc.* **2011**, *133*, 14160.
[39] J. I. Steinfeld, J. S. Francisco, W. L. Hase, *Chemical Kinetics and Dynamics*, 2nd ed., Prentice-Hall, Englewood Cliffs, NJ **1999**.
[40] *Datasheet of tryphenilalanine (FFF) powder*, Bachem (Switzerland).
[41] M. Gil, M. Kijak, H. Piwoński, J. Herbich, J. Waluk, *Methods Appl. Fluoresc.* **2017**, *5*, 014007.
[42] S. K. Joseph, N. Kuritz, E. Yahel, N. Lapshina, G. Rosenman, A. Natan, **2018**, preprint: arXiv:1808.03262.
[43] L. Adler-Abramovich, E. Gazit, *Chem. Soc. Rev.* **2014**, *43*, 6881.
[44] Y. Svenskaya, B. Parakhonskiy, A. Haas, V. Atkin, E. Lukyanets, D. Gorin, R. Antolini, *Biophys. Chem.* **2013**, *182*, 11.
[45] B. V. Parakhonskiy, C. Foss, E. Carletti, M. Fedel, A. Haase, A. Motta, C. Migliaresi, R. Antolini, *Biomater. Sci.* **2013**, *1*, 1273.